Measurement of L-Shell Emission from Iron-Group Elements for High-Resolution X-Ray Spectroscopy in Future Astronomy*)

Yuken OHSHIRO[1,2)], Tomoko KAWATE[3,4)], Hiroya YAMAGUCHI[2,1)] and Izumi MURAKAMI[3,4)]

[1)]*Department of Physics, Graduate School of Science, The University of Tokyo, 7-3-1 Hongo, Bunkyo-ku, Tokyo 113-0033, Japan*

[2)]*Institute of Space and Astronautical Science (ISAS), Japan Aerospace Exploration Agency (JAXA), 3-1-1 Yoshinodai, Chuo-ku, Sagamihara, Kanagawa 252-5210, Japan*

[3)]*National Institute for Fusion Science, National Institutes of Natural Sciences, 322-6 Oroshi-cho, Toki, Gifu 509-5292, Japan*

[4)]*Department of Fusion Science, The Graduate University for Advanced Studies, SOKENDAI, 322-6 Oroshi-cho, Toki, Gifu 509-5292, Japan*

(Received 9 January 2023 / Accepted 23 March 2023)

Measuring abundance of iron-group elements (IGEs; Cr, Mn, Fe, and Ni) is essential for understanding astrophysical phenomena such as supernovae. The L-shell emissions from IGEs will soon be resolved by next-generation X-ray satellites, enabling more accurate measurements of abundance. However, theoretical calculations for these L-shell transitions have not been sufficiently validated using experimental work. Herein, large helical device (LHD) experiments that measured L-shell emission from Ni and Mn are reported. The temporal evolution of LHD plasma is characterized by three phases, each of which resolves different L-shell emissions. We modeled EUV-Short spectra considering LHD plasma structure with AtomDB, an atomic database widely used in the X-ray astronomy community. We discovered that the observed intensity ratios of the 3C ($2p^5 3d^1\ ^1P_1 \rightarrow 2p^6\ ^1S_0$) to 3D ($2p^5 3d^1\ ^3D_1 \rightarrow 2p^6\ ^1S_0$) transition of Ne-like ions are 0.4 - 0.6 times lower than the theoretically predicted ratios.

Keywords: EUV spectroscopy, line identification, intensity ratio, nickel, manganese

DOI: 10.1585/pfr.18.2401041

1. Introduction

The measurement of elemental abundance in various astrophysical objects is essential for understanding the origin and chemical evolution of the universe. In particular, the abundance of iron-group elements (IGEs), such as Cr, Mn, Fe, and Ni, in supernova remnants (SNRs), is crucial in revealing how their progenitors evolve and explode [1, 2]. The SNR structure is formed 100 - 1000 years after a supernova and contains hot thermal collision plasma comprising elements synthesized in a supernova. SNR plasma is an optically thin thermal collisional plasma with an electron temperature of a few keV and an electron density of $\sim 1\,\mathrm{cm}^{-3}$. Because of the low electron density, the SNR plasmas frequently undergo nonequilibrium ionization, and the IGEs remain in intermediate charge states (e.g., Fe^{16+}) [3]. To accurately measure the abundance of IGEs in such a condition, precise measurements of the electron temperature and ionization state are required.

After August 2023, the X-ray astronomy satellite XRISM will be launched by JAXA, enabling high-resolution X-ray spectroscopy [4]. The X-ray microcalorimeter onboard XRISM has an order of magnitude higher energy resolution ($\Delta E \sim 5\,\mathrm{eV}$ @ $6.4\,\mathrm{keV}$) than the previous charge-coupled device (CCD) detector, enabling the resolution of various emissions, including K- and L-shell emissions from IGEs with different charge states. These emission lines enable detailed plasma diagnostics, improve the accuracy of electron temperature and ionization state measurements, and reduce the systematic uncertainty of elemental abundance. However, high-resolution X-ray spectroscopy poses some difficulties. Collisional radiative modeling based on atomic data, such as energy levels and transition probabilities of transition processes, is essential for accurately interpreting X-ray spectra. However, only a few atomic data have been evaluated via laboratory experiments. This study presents laboratory experiments conducted at the National Institute for Fusion Science using a large helical device (LHD) to measure L-shell emissions from IGEs. The experimental setup is described in Section 2, data analysis and line identifications are presented in Section 3, a discussion based on spectrum synthesis using the atomic database, AtomDB [5], which is widely used in X-ray astronomy, is presented in Section 4, and a summary is presented in Section 5.

author's e-mail: ohshiro-yuken@g.ecc.u-tokyo.ac.jp

*) This article is based on the presentation at the 31st International Toki Conference on Plasma and Fusion Research (ITC31).

2. Experimental Setup

LHD is a heliotron-type plasma confinement device [6]. Herein, the major and minor radii were set to 3.6 m and 0.64 m, respectively, and the toroidal magnetic field was set to 2.75 T. Two extreme ultraviolet (EUV) spectrometers, EUV-Short and EUV-Short2, were used [7]. The former was used for spectroscopy of L-shell emissions, while the latter was used to determine the spatial distribution of L-shell emissions. Back-illuminated CCD detectors were installed at the exit slits of each spectrometer. The CCD measures 26.6 mm × 6.6 mm and has 1024 × 255 pixels. The spectral resolution of each spectrometer is ~ 0.08 Å at 33.73 Å [7]. A schematic of the spectroscopy system is shown in Fig. 1 of ref. [8]. EUV-Short and EUV-Short2 cover the center and upper half of the LHD plasma, respectively.

In the impurity experiments described in the following section, Ni and Mn from IGEs were selected as impurities because a previous study used Fe [9] and there are technical difficulties with Cr. Ni and Mn were injected into the LHD plasma using a coaxial carbon pellet [10] and a tracer-encapsulated solid pellet [11, 12], respectively. In addition, Ne and N_2 gas injection experiments were conducted for wavelength calibration. The LHD plasma was heated using electron cyclotron heating (ECH) and neutral beam injection (NBI). The radial profiles of electron temperature and density were measured using Thomson scattering and Michelson interferometry with a far-infrared CH_3OH laser (119 μm). Wavelength ranges of 5 - 47 Å and 8 - 17 Å were covered by the spectrometers EUV-Short and EUV-Short2, respectively. For EUV-Short, a time resolution of 5 ms and full vertical binning mode were used. For EUV-Short2, a time resolution of 100 ms was used and the wavelength channels were binned to obtain a good signal-to-noise ratio. This study used well-known lines, such as C, N, O, Ne, and Fe, for wavelength calibration. The bremsstrahlung continuum and its wavelength dependence were used for relative intensity calibration (details of the method are presented in [7]).

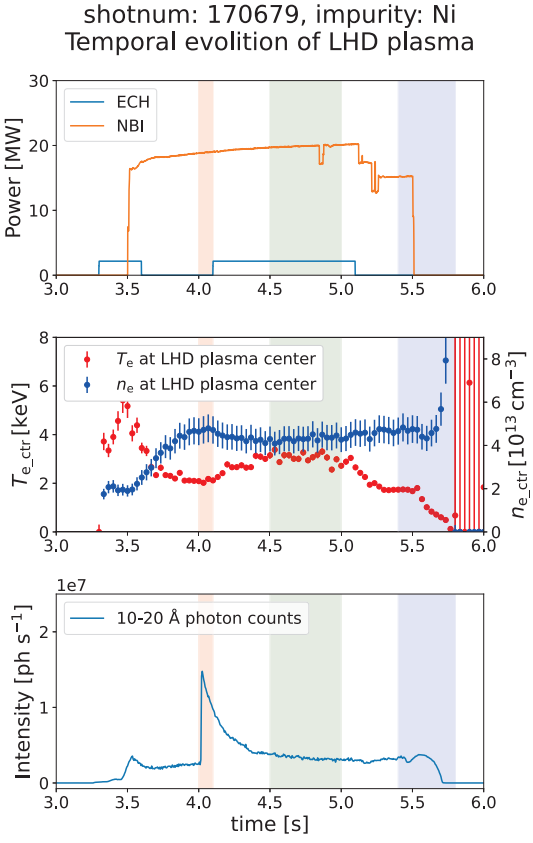

Fig. 1 Temporal evolution of the LHD plasma in Ni injection experiment. The injection power, the electron temperature (red dots) and density (blue dots), and the 10 - 20 Å photon counts are shown in (a), (b), and (c), respectively.

3. Temporal Analysis of the LHD Plasma

Temporal evolution of the (a) heating power of ECH and NBI, (b) electron temperature and electron density at the LHD plasma center, and (c) total photon counts of EUV-Short in the range of 10 - 20 Å are shown in Fig. 1 (shot number: 170679, impurity: Ni). The plasma was initiated by ECH and heated further by NBI, increasing the electron temperature to ~ 2 keV. When the impurity was injected at t = 4.0 s, the photon counts increased rapidly. ECH was superimposed between t = 4.1 - 5.1 s to prevent radiative collapse owing to the rapid increase in radiative loss caused by impurity injection. After 0.5 seconds of impurity injection, the photon counts stabilized. All heating sources were turned off at t = 5.5 s, causing the electron temperature to decrease. In addition, photon counts varied in response to changes in electron temperature. Based on the LHD plasma behavior, three characteristic phases were defined as follows: (1) ionizing phase: immediately after impurity injection (red region in Fig. 1); (2) equilibrium phase: total photon counts, electron temperature, and electron density are stable (green region in Fig. 1); (3) recombining phase: when the electron temperature is decreasing (blue region in Fig. 1).

Figure 2 shows the accumulated EUV-Short spectra in three phases for (a) Ni and (b) Mn injection. Various L-shell emissions were detected in the 8 - 20 Å wavelength range. The L-shell emissions were identified based on two atomic databases, AtomDB and NIST [13]. For Ni, L-shell emissions from Li- to Ne-like ions have been identified in the 8 - 15 Å wavelength range. L-shell emissions from the intermediate charge state, such as Ni XIX 3C (12.44 Å), 3D (12.65 Å), 3F (13.79 Å), and 3G+M2 (14.07 Å), have been identified in the ionizing and recombining phases. L-shell emissions from the highly charged state, such as Ni XXVI, Ni XXV, and Ni XXIV, have been identified in the equilibrium phase. For Mn, L-shell emissions from Li- to Ne-like ions have been observed in the wavelength range of 8 - 20 Å. L-shell emissions from the intermediate charge state, such as Mn XVI 3C (16.64 Å), 3D (16.89 Å), 3F (18.67 Å), and 3G+M2 (18.97 Å), have been identified in the recombining phase. L-shell emissions from the highly

charged state, such as Mn XXIII and Mn XXII, have been identified in the equilibrium phase. In addition, transitions from high-n levels have been identified in the equilibrium phase ~ 9 Å.

The central wavelengths of the identified lines were measured using Gaussian fitting. The results are summarized in Table 1. The wavelength uncertainties in the table represent the quadrature sum of calibration errors of 5 mÅ, CCD channel intervals of 19 mÅ for Ni XIX and 20 mÅ for Mn XVI, and estimated statistical uncertainties ranging from 2 to 8 mÅ. The complete list of identified lines is presented in the Appendix.

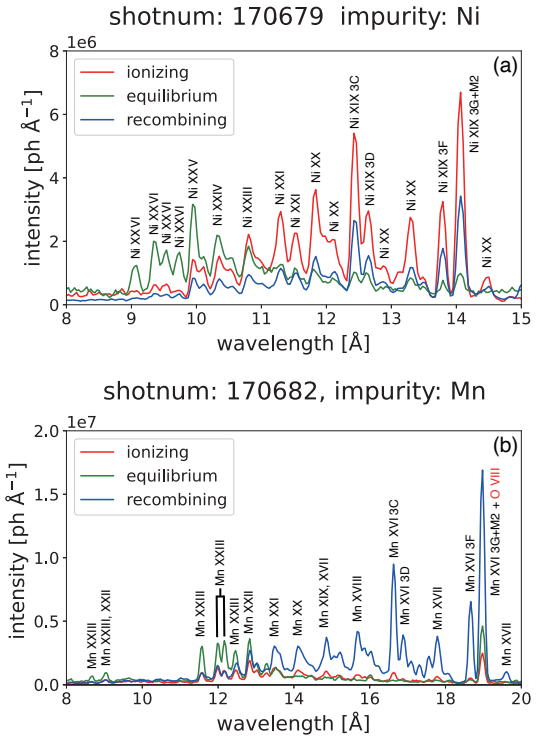

Fig. 2 EUV-Short spectra of (a) Ni and (b) Mn. Each panel shows the accumulated spectra in the ionizing phase (solid red line), the equilibrium phase (solid green line), and the recombining phase (solid blue line).

Table 1 Identified L-shell emissions.

		Wavelength [Å]		
Name	Transition	This work	AtomDB	NIST
Ni XIX 3C	$2p^5 3d\,^1P_1 \rightarrow 2p^6\,^1S_0$	12.44 ± 0.02	12.435	12.432
Ni XIX 3D	$2p^5 3d\,^3D_1 \rightarrow 2p^6\,^1S_0$	12.65 ± 0.02	12.656	12.654
Ni XIX 3F	$2p^5 3s\,^3P_1 \rightarrow 2p^6\,^1S_0$	13.79 ± 0.02	13.779	13.780
Ni XIX 3G	$2p^5 3s\,^1P_1 \rightarrow 2p^6\,^1S_0$	14.07 ± 0.02	14.043	14.043
Ni XIX M2	$2p^5 3s\,^3P_2 \rightarrow 2p^6\,^1S_0$		14.077	14.078
Mn XVI 3C	$2p^5 3d\,^1P_1 \rightarrow 2p^6\,^1S_0$	16.64 ± 0.02	16.679	16.616
Mn XVI 3D	$2p^5 3d\,^3D_1 \rightarrow 2p^6\,^1S_0$	16.89 ± 0.02	16.951	16.882
Mn XVI 3F	$2p^5 3s\,^3P_1 \rightarrow 2p^6\,^1S_0$	18.67 ± 0.02	18.741	18.654
Mn XVI 3G	$2p^5 3s\,^1P_1 \rightarrow 2p^6\,^1S_0$	18.97 ± 0.02	19.023	18.935
Mn XVI M2	$2p^5 3s\,^3P_2 \rightarrow 2p^6\,^1S_0$		19.073	-

4. Modeling the EUV-Short Spectrum Based on the LHD Plasma Structure

In the previous section, we identified the L-shell emissions from Ne-like ions and measured the central wavelengths using two atomic databases. The observed wavelengths of Ni emissions are consistent with astrophysical X-ray observations [14] and other laboratory experiments [15]. However, the observed wavelengths of Mn emissions are ~ 50 mÅ shorter than AtomDB values but consistent with NIST values. This is because the NIST values were calibrated by a previous study measuring Mn XVI emission through vacuum discharge [16], whereas the AtomDB value is calculated by flexible atomic code [17].

The EUV-Short spectrum was modeled based on the LHD plasma structure using the collisional radiative model implemented in AtomDB and compared it to the observed spectrum. To calculate the LHD plasma structure, we made the following two assumptions: (1) The electron temperature, density, and impurity are symmetrically distributed based on magnetic coordinates. (2) The LHD plasma is in collisional ionization equilibrium in any observed frame. To determine the spatial structure of LHD plasmas, a good signal-to-noise ratio of the EUV-Short2 spectrum is required. In the recombining phase, the EUV-Short2 spectrum with a good signal-to-noise ratio was obtained owing to the absence of NBI, which is the main source of the noise. In addition, various L-shell emissions are detected in the recombining phase, as mentioned in Section 3. Therefore, we focus on the analysis of frames with $t = 5.6$ s.

Figures 3 (a) and (b) show the electron temperature and density distributions at $t = 5.6$ s, respectively. Temperature and density distributions were mapped in the plasma cross-section, including the vertical observation range of EUV-Short2. The distributions of electron temperature and density in the magnetic coordinates were obtained from `tsmap`, whereas the magnetic coordinates at plasma cross-

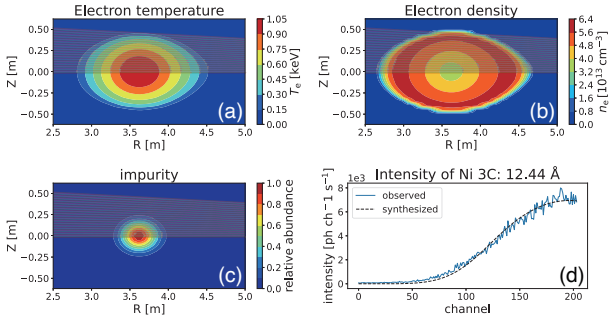

Fig. 3 The distribution of (a) electron temperature, (b) electron density, and (c) impurity. Line-of-sights of each channel of EUV-Short2 are also plotted. (d) shows the Ni XIX 3C intensity distribution. observed and synthesized distribution are plotted in blue solid line and black solid line, respectively.

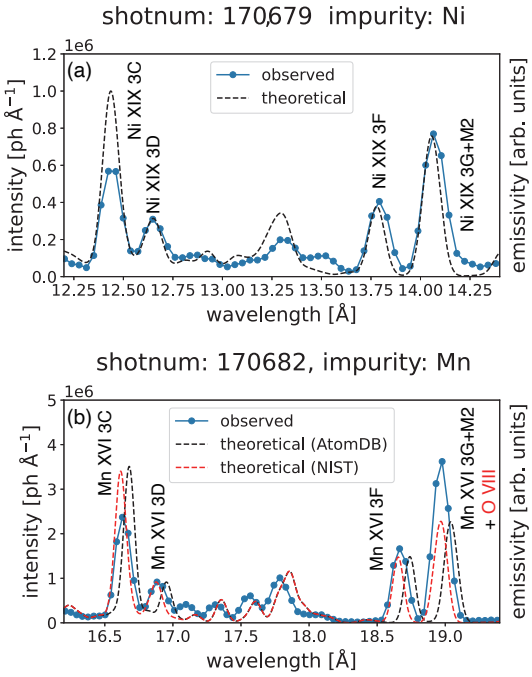

Fig. 4 Comparison between observed (blue solid line) and theoretical (black dashed line) spectrum of (a) Ni and (b) Mn. The solid red line in the bottom panel shows the theoretical spectrum with the central wavelengths of Ne-like transitions (i.e., 3C, 3D, 3F, 3G, and M2) replaced with the NIST values.

section were obtained from `tsmesh_h` in the LHD experiment data repository[1]. We cannot directly measure the relationship between impurity distribution and magnetic coordinates. Therefore, we mapped the impurity distribution in real coordinates, assuming that the impurity is distributed with a Gaussian function in the minor radius of the magnetic coordinate. We then calculated the theoretical intensity distribution with an impurity distribution and integrated it with the line-of-sight of each EUV-Short2 channel. Further, we fitted the impurity distribution to reproduce the intensity distribution observed by EUV-Short2 with the peak, width, and normalization factor of the Gaussian function as free parameters. We used the intensity distribution of Ni XIX 3C (or Mn XVI 3C) for fitting because both emissions are strongest in the EUV-Short2 observation range. The fitted impurity distribution and a comparison between the calculated and observed Ni XIX 3C intensity distributions at t = 5.6 s are shown in Figs. 3 (c) and (d), respectively.

Figure 4 shows the observed (blue solid line) and theoretical (black dashed line) EUV-Short spectra of (a) Ni and (b) Mn experiments. The theoretical EUV-Short spectrum was synthesized using estimated LHD plasma distribution, as described in the previous paragraph. In this wavelength range, emission lines from Ne-like and more highly charged ions are detected (Fig. 4). Because we inferred the impurity distribution using their emission, only the Ne-like ions are discussed herein. The observed spectra indicated that the 3C/3D intensity ratios of Ni and Mn are significantly lower than the theoretical predictions. These discrepancies are not believed to be due to calibration uncertainty because the relative efficiency over the discussed wavelength range has been well calibrated using the bremsstrahlung continuum (Section 2). Further, no strong emission is predicted around the 3C and 3D emissions, so contamination from other emissions is unlikely. However, the O VIII Lyα emission is predicted to appear at 18.97 Å, which may be responsible for the observed excessive Mn XVI 3G+M2 emission. Notably, the collisional radiative model implemented in AtomDB employs a low electron density limit approximation (so-called corona approximation). During our experiments, the typical electron density of LHD plasma was (1 - 5) $\times 10^{13}$ cm^{-3}, which is significantly higher than the assumed value of the model. Therefore, we used Atomic Data and Analysis Structure (ADAS [18]) to investigate the effect of electron density. Consequently, we confirmed that the intensity ratio of 3C to 3D changes by no more than 5% from the value when the corona approximation is assumed. The observed and theoretical 3C/3D ratios of Ni XIX are 1.43 ± 0.11 and 3.57, respectively. The observed ratio is 0.4 times lower than the theoretical value. Previous laboratory or astrophysical measurements show that the measured 3C/3D ratios [19–21], ranging from 2.12 - 2.35, are consistent with the presented ratio. For Mn, the observed and theoretical 3C/3D ratios of Mn XVI are 2.49 ± 0.29 and 4.01, respectively. The observed ratio is 0.6 times lower than the theoretical value. Previous laboratory measurements were conducted using electron beam ion trap experiments [19], and the 3C/3D ratio is 3.42 ± 0.30, which is inconsistent with the observed ratio. However, the trend is consistent with the measured 3C/3D ratio being less than the theoretical value. The 3C/3D ratio has long been debated, particularly in Fe XVII. Recent measurements using an electron beam ion trap and monochromatic X-ray synchrotron radiation have enabled direct measurement of the 3C/3D oscillator-strength ratio [22]. The measured 3C/3D oscillator-strength ratio is consistent with the state-of-the-art theoretical predictions. Therefore, both experimental and theoretical efforts are required to solve the 3C/3D ratio problem for Ni and Mn.

5. Summary

We measured L-shell emission from Ni and Mn using LHD impurity injection experiments. We identified various L-shell emissions from Li- to Ne-like ions. We also modeled the EUV-Short spectrum using the atomic database, AtomDB, based on the LHD plasma structure and compared it to the observed spectrum. The observed intensity ratios for 3C ($2p^5 3d^1\,{}^1P_1 \rightarrow 2p^6\,{}^1S_0$) and 3D ($2p^5 3d^1\,{}^3D_1 \rightarrow 2p^6\,{}^1S_0$) are 0.4 - 0.6 times lower than the

[1]https://www-lhd.nifs.ac.jp/pub/Repository_en.html

predicted value.

Acknowledgement

The authors would like to thank all the members of the LHD experiment group for their cooperation, including technical support. This work is supported by Grants-in-Aid for Scientific Research (KAKENHI) of the Japanese Society for the Promotion of Science grant No. JP22J21194 (Y.O.). This work is also supported by the NIFS Collaboration Research Program (NIFS20KLPF076).

Appendix: Complete List of Identified Lines

The complete list of identified lines is presented in Table A. The wavelength uncertainties in the table represent the quadrature sum of calibration errors of 5 mÅ, the interval of the CCD channel, which range from 16 - 22 mÅ, and estimated statistical uncertainties, which range from 2 - 15 mÅ.

Table A Identified L-shell emissions. The asterisk symbols indicate the emission line overlaps with other transitions.

		Wavelength [Å]			
Ion	transition	This work	AtomDB	NIST	previous measurement
Ni XXVI*	$1s^2 3p\,^2P_{3/2} \rightarrow 1s^2 2s\,^2S_{1/2}$	9.05 ± 0.02	9.060	9.060	-
Ni XXVI*	$1s^2 3d\,^2D_{3/2} \rightarrow 1s^2 2p\,^2P_{1/2}$	9.36 ± 0.02	9.385	9.385	-
Ni XXVI	$1s^2 3d\,^2D_{5/2} \rightarrow 1s^2 2p\,^2P_{3/2}$	9.55 ± 0.02	9.529	9.529	-
Ni XXVI	$1s^2 3s\,^2S_{1/2} \rightarrow 1s^2 2p\,^2P_{3/2}$	9.73 ± 0.02	9.745	9.745	-
Ni XXV*	$1s^2 2s3d\,^1D_2 \rightarrow 1s^2 2s2p\,^1P_1$	9.95 ± 0.02	-	9.968	9.97 [23]
Ni XXI	$1s^2 2p^3(^2D)3d\,^3D_3 \rightarrow 2s^2 2p^4\,^3P_2$	11.30 ± 0.02	11.318	11.319	11.318 [24]
Ni XIX	$2s2p^6 3p\,(1/2, 3/2)_3 \rightarrow 2s^2 2p^6\,^1S_0$	11.53 ± 0.02	11.539	11.537	11.537 [15]
Ni XX	$2s^2 2p^4 3d\,^2D_{5/2} \rightarrow 2s^2 2p^5\,^2P_{3/2}$	11.82 ± 0.02	11.832	11.831	11.831 [15]
Ni XIX 3C	$2p^5 3d\,^1P_1 \rightarrow 2p^6\,^1S_0$	12.44 ± 0.02	12.435	12.432	12.432 [15]
Ni XIX 3D	$2p^5 3d\,^3D_1 \rightarrow 2p^6\,^1S_0$	12.65 ± 0.02	12.656	12.654	12.654 [15]
Ni XX	$2s^2 2p^4(^2D)3s\,^2D_{5/2} \rightarrow 2s^2 2p^5\,^2P_{3/2}$	12.89 ± 0.02	12.927	12.930	12.930 [15]
Ni XX*	$2s^2 2p^4(^2D)3s\,^2D_{3/2} \rightarrow 2s^2 2p^5\,^2P_{3/2}$	13.31 ± 0.02	13.075	13.078	13.078 [15]
Ni XX*	$2s^2 2p^4(^3P)3s\,^4P_{5/2} \rightarrow 2s^2 2p^5\,^2P_{3/2}$	13.51 ± 0.02	13.309	13.310	13.310 [15]
Ni XIX 3F	$2p^5 3s\,^3P_1 \rightarrow 2p^6\,^1S_0$	13.79 ± 0.02	13.779	13.780	13.780 [15]
Ni XIX 3G	$2p^5 3s\,^1P_1 \rightarrow 2p^6\,^1S_0$	14.07 ± 0.02	14.043	14.043	14.042 [15]
Ni XIX M2	$2p^5 3s\,^3P_2 \rightarrow 2p^6\,^1S_0$		14.077	14.078	14.080 [15]
Mn XXIII*	$1s^2 4p\,^2P_{3/2} \rightarrow 1s^2 2s\,^2S_{1/2}$	8.66 ± 0.02	8.689	8.689	-
Mn XXIII*	$1s^2 3p\,^2P_{3/2} \rightarrow 1s^2 2s\,^2S_{1/2}$	11.57 ± 0.02	11.553	11.553	-
Mn XXIII	$1s^2 3d\,^2D_{3/2} \rightarrow 1s^2 2p\,^2P_{1/2}$	11.99 ± 0.02	12.019	12.019	-
Mn XXIII	$1s^2 3d\,^2D_{5/2} \rightarrow 1s^2 2p\,^2P_{3/2}$	12.17 ± 0.02	12.163	12.163	-
Mn XXIII	$1s^2 3d\,^2D_{5/2} \rightarrow 1s^2 2p\,^2P_{3/2}$	12.47 ± 0.02	12.444	12.444	-
Mn XVI	$2s^2 2p^5(^2D_{1/2})4d\,^2[2/3]_1 \rightarrow 2s^2 2p^6\,^1S_0$	13.48 ± 0.02	13.481	13.461	13.46 [16]
Mn XVI	$2s^2 2p^5(^2D_{3/2})4d\,^2[2/3]_1 \rightarrow 2s^2 2p^6\,^1S_0$	13.62 ± 0.02	13.626	13.615	13.61 [16]
Mn XVIII	$2s^2 2p^3(^2D)3d\,^3D_3 \rightarrow 2s^2 2p^4\,^3D_2$	14.86 ± 0.02	14.898	14.877	-
Mn XVIII	$2s^2 2p^3(^2D)3d\,^3D_3 \rightarrow 2s^2 2p^4\,^3D_2$	15.23 ± 0.03	15.212	15.238	-
Mn XVII*	$2s^2 2p^4(^1D)3d\,^2D_{5/2} \rightarrow 2s^2 2p^5\,^2P_{3/2}$	15.69 ± 0.02	15.707	15.670	15.670 [25]
Mn XVI 3C	$2p^5 3d\,^1P_1 \rightarrow 2p^6\,^1S_0$	16.64 ± 0.02	16.679	16.616	16.616 [16]
Mn XVI 3D	$2p^5 3d\,^3D_1 \rightarrow 2p^6\,^1S_0$	16.89 ± 0.02	16.951	16.882	16.882 [16]
Mn XVII	$2s^2 2p^4(^2D)3s\,^2D_{5/2} \rightarrow 2s^2 2p^5\,^2P_{3/2}$	17.31 ± 0.02	17.356	17.300	17.301 [25]
Mn XVII*	$2s^2 2p^4(^2D)3s\,^2D_{3/2} \rightarrow 2s^2 2p^5\,^2P_{3/2}$	17.56 ± 0.02	17.603	17.550	17.550 [25]
Mn XVII*	$2s^2 2p^4(^3P)3s\,^4P_{5/2} \rightarrow 2s^2 2p^5\,^2P_{3/2}$	17.79 ± 0.02	17.855	17.794	17.794 [25]
Mn XVI 3F	$2p^5 3s\,^3P_1 \rightarrow 2p^6\,^1S_0$	18.67 ± 0.02	18.741	18.654	18.654 [16]
Mn XVI 3G	$2p^5 3s\,^1P_1 \rightarrow 2p^6\,^1S_0$	18.97 ± 0.02	19.023	18.935	18.935 [16]
Mn XVI M2	$2p^5 3s\,^3P_2 \rightarrow 2p^6\,^1S_0$		19.073	-	-

[1] Y. Ohshiro, H. Yamaguchi, S.-C. Leung, K. Nomoto, T. Sato, T. Tanaka, H. Okon, R. Fisher, R. Petre and B.J. Williams, Discovery of a Highly Neutronized Ejecta Clump in the Type Ia Supernova Remnant 3C 397, Astrophys. J. Lett. **913** (2), L34 (June 2021).

[2] T. Sato, K. Maeda, S. Nagataki, T. Yoshida, B. Grefenstette, B.J. Williams, H. Umeda, M. Ono and J.P. Hughes, High-entropy ejecta plumes in Cassiopeia A from neutrino-driven convection, Nature **592** (7855), 537 (April 2021).

[3] H. Yamaguchi, C. Badenes, R. Petre, T. Nakano, D. Castro, T. Enoto, J.S. Hiraga, J.P. Hughes, Y. Maeda, M. Nobukawa, S. Safi-Harb, P.O. Slane, R.K. Smith and H. Uchida, Discriminating the Progenitor Type of Supernova Remnants with Iron K-Shell Emission, Astrophys. J. **785** (2), L27 (April 2014).

[4] XRISM Science Team, Science with the X-ray Imaging and Spectroscopy Mission (XRISM), arXiv e-prints, 2003:arXiv:2003.04962 (March 2020).

[5] A.R. Foster, L. Ji, R.K. Smith and N.S. Brickhouse, Updated Atomic Data and Calculations for X-Ray Spectroscopy, Astrophys. J. **756** (2), 128 (August 2012).

[6] A. Iiyoshi, A. Komori, A. Ejiri, M. Emoto, H. Funaba, M. Goto, K. Ida, H. Idei, S. Inagaki, S. Kado, O. Kaneko, K. Kawahata, T. Kobuchi, S. Kubo, R. Kumazawa, S. Masuzaki, T. Minami, J. Miyazawa, T. Morisaki, S. Morita, S. Murakami, S. Muto, T. Mutoh, Y. Nagayama, Y. Nakamura, H. Nakanishi, K. Narihara, K. Nishimura, N. Noda, S. Ohdachi, N. Ohyabu, Y. Oka, M. Osakabe, T. Ozaki, B. J. Peterson, A. Sagara, S. Sakakibara, R. Sakamoto, H. Sasao, M. Sasao, K. Sato, M. Sato, T. Seki, T. Shimozuma, M. Shoji, H. Suzuki, Y. Takeiri, K. Tanaka, K. Toi, T. Tokuzawa, K. Tsumori, K. Tsuzuki, K. Y. Watanabe, T. Watari, H. Yamada, I. Yamada, S. Yamaguchi, M. Yokoyama, R. Akiyama, H. Chikaraishi, K. Haba, S. Hamaguchi, M. Iima, S. Imagawa, N. Inoue, K. Iwamoto, S. Kitagawa, J. Kodaira, Y. Kubota, R. Maekawa, T. Mito, T. Nagasaka, A. Nishimura, C. Takahashi, K. Takahata, Y. Takita, H. Tamura, T. Tsuzuki, S. Yamada, K. Yamauchi, N. Yanagi, H. Yonezu, Y. Hamada, K. Matsuoka, K. Murai, K. Ohkubo, I. Ohtake, M. Okamoto, S. Satoh, T. Satow, S. Sudo, S. Tanahashi, K. Yamazaki, M. Fujiwara and O. Motojima, Overview of the Large Helical Device project, Nucl. Fusion **39** (9Y), 1245 (September 1999).

[7] M.B. Chowdhuri, S. Morita and M. Goto, Characteristics of an absolutely calibrated flat-field extreme ultraviolet spectrometer in the 10-130 A range for fusion plasma diagnostics, Applied Optics **47** (2), 135 (January 2008).

[8] T. Oishi, N. Ashikawa, F. Nespoli, S. Masuzaki, M. Shoji, E.P. Gilson, R. Lunsford, S. Morita, M. Goto, Y. Kawamoto, C. Suzuki, Z. Sun, A. Nagy, D.A. Gates and T. Morisaki, Line identification of boron and nitrogen emissions in extreme- and vacuum-ultraviolet wavelength ranges in the impurity powder dropping experiments of the Large Helical Device and its application to spectroscopic diagnostics, Plasma Sci. Technol. **23** (8), 084002 (June 2021).

[9] X.L. Huang, E.H. Wang, C.F. Dong, S. Morita, T. Oishi, I. Murakami and M. Goto, Radial profiles and emissivity ratio analysis of Ne-like FeXVII n = 3-2 transitions in Large Helical Device, J. Korean Physical Society **65** (8), 1265 (October 2014).

[10] H. Nozato, S. Morita, M. Goto, A. Ejiri and Y. Takase, Acceleration characteristics of spherical and nonspherical pellets by the LHD impurity pellet injector, Rev. Sci. Instrum. **74** (3), 2032 (March 2003).

[11] K.V. Khlopenkov and S. Sudo, Production and acceleration of tracer encapsulated solid pellets for particle transport diagnostics, Rev. Sci. Instrum. **69** (9), 3194 (September 1998).

[12] S. Sudo, N. Tamura, S. Muto, T. Ozaki, C. Suzuki, H. Funaba, I. Murakami, D. Kato, S. Inagaki and Katsumi Ida, Plasma Diagnostics with Tracer-Encapsulated Solid Pellet, Plasma Fusion Res. **9**, 1402039 (2014).

[13] A. Kramida, Yu. Ralchenko, J. Reader and and NIST ASD Team, NIST Atomic Spectra Database (ver. 5.10), [Online]. Available: https://physics.nist.gov/asd [2022, December 21]. National Institute of Standards and Technology, Gaithersburg, MD., 2022.

[14] E. Behar, J. Cottam and S.M. Kahn, The Chandra Iron-L X-Ray Line Spectrum of Capella, Astrophys. J. **548** (2), 966 (February 2001).

[15] M.F. Gu, P. Beiersdorfer, G.V. Brown, H. Chen, D.B. Thorn and S.M. Kahn, Wavelength Measurements of Ni L-Shell Lines between 9 and 15 A, Astrophys. J. **657** (2), 1172 (March 2007).

[16] F. Tyrén, Die optischen L-Spektren der Elemente Chrom bis Kobalt im extremen Ultraviolett, Zeitschrift für Physik **111** (5), 314 (May 1938).

[17] M.F. Gu, The flexible atomic code, Canadian Journal of Physics **86** (5), 675 (May 2008).

[18] H.P. Summers. The ADAS User Manual, version 2.6. https://www.adas.ac.uk/manual.php.

[19] G.V. Brown, P. Beiersdorfer and K. Widmann, Phys. Rev. A **63** (3), 032719 (February 2001).

[20] M.F. Gu, P. Beiersdorfer, G.V. Brown, H. Chen, K.R. Boyce, R.L. Kelley, C.A. Kilbourne, F.S. Porter and S.M. Kahn, Laboratory Measurements of $3 \rightarrow 2$ X-Ray Emission Lines of Ne-like Ni XIX, Astrophys. J. **607** (2), L143 (April 2004).

[21] D.L. McKenzie, P.B. Landecker, R.M. Broussard, H.R. Rugge, R.M. Young, U. Feldman and G.A. Doschek, Solar flare X-ray spectra between 7.8 and 23.0 Angstroms, Astrophys. J. **241**, 409 (October 1980).

[22] S. Kühn, C. Cheung, N.S. Oreshkina, R. Steinbrügge, M. Togawa, S. Bernitt, L. Berger, J. Buck, M. Hoesch, J. Seltmann, F. Trinter, C.H. Keitel, M.G. Kozlov, S.G. Porsev, M.F. Gu, F.S. Porter, T. Pfeifer, M.A. Leutenegger, Z. Harman, M.S. Safronova, J.R. Crespo López-Urrutia and C. Shah, New Measurement Resolves Key Astrophysical Fe XVII Oscillator Strength Problem, Phys. Rev. Lett. **129** (24), 245001 (December 2022).

[23] B.C. Fawcett, A. Ridgeley and T.P. Hughes, Line classifications for Ni XXV and XXVI and new observations of Fe XXIII and XXIV in laser-produced spectra, Monthly Notices of the Royal Astronomical Society **188** (2), 365 (September 1979).

[24] H. Gordon, M.G. Hobby and N.J. Peacock, Classification of the X-ray spectra of transitions in the Ne, F and O I isoelectronic sequences of the elements from iron to bromine and in the Na I isoelectronic sequence of gallium to bromine, J. Phys. B: Atomic and Molecular Physics **13** (10), 1985 (May 1980).

[25] U. Feldman, G.A. Doschek, R.D. Cowan and L. Cohen, Fluorine isoelectronic sequence, JOSA **63** (11), 1445 (November 1973).